In-situ imaging of flexure-induced fracture in tape-laminate composites using high-resolution X-ray computed tomography

Brian P. Wingate and Michael W. Czabaj*
Department of Mechanical Engineering, University of Utah, Salt Lake City, Utah 84112, USA
*Corresponding author: m.czabaj@utah.edu

ABSTRACT

This study presents development of an in-situ flexure test for imaging progressive inter- and intralaminar fracture in tape-laminate composites using X-ray computed tomography (CT). The intent of this test is to provide detailed experimental observations of ply-level damage that can be used to validate existing, and develop new, progressive damage analysis (PDA) tools. The test consists of a vertically mounted specimen which is flexed using two eccentric compressive loads using an in-situ uniaxial load stage. The flexure specimen contains a starter notch mid-span which promotes initiation of composite failure within the X-ray field of view. Specimens with two different laminate stacking sequences were tested, imaged, analyzed. For a quasi-isotropic laminate with large angle changes between adjacent plies, there was near simultaneous growth of transverse cracks and delaminations below the midplane of the laminate. For a laminate with small angles between adjacent plies, there was extensive formation of transverse crack networks which penetrated the laminate thickness without delamination growth. In addition to imaging fracture, the X-ray CT data from both specimen types were used to quantify the variability in thickness and analyze the local orientation of individual plies. Overall, the proposed test and the image-data analysis methodology provided an important insight into the fracture processes in tape laminates and highlights the inherent ply-level geometrical variabilities that should be accounted for in PDA simulations.

Keywords: computed tomography, damage evolution, tape-laminate composites, model validation

1. Introduction

Recent developments in progressive-damage analysis (PDA) tools based on finite element (FE) methods have enabled simulation of complex fracture patterns observed in tape-laminate fiber-reinforced composites (FRCs). To date, PDA tools have been developed to simulate the initiation, growth, and interaction of intralaminar transverse cracks and delaminations under a variety of static and fatigue loading conditions. A few notable examples of these approaches include the Floating Node Method [1], the Regularized Extended-Finite Element Method [2], and the Augmented Finite Element Method [3]. Given the ongoing development of these methods, and their increasing acceptance within the composites engineering community, there exists an ever-growing need for new and detailed experiments to evaluate their predictive accuracy and guide their future development.

The predictive capability of PDA tools is commonly evaluated by directly comparing the simulated results to those obtained from progressive-damage experiments (e.g., open-hole tension tests, indentation tests, etc.). PDA results can be compared to experimental data either by directly comparing the global structural response of a test article during damage evolution, or by comparing the final state of simulated and experimentally-observed damage. The latter approach typically involves post-mortem examination of the damage in test articles. Detailed information about the damage state may be obtained using serial sectioning coupled with scanning-electron or optical microscopy [4], ultrasonic inspection [5-8], 2D X-ray radiography [9,10], or ex-situ 3D X-ray computed tomography (CT) [11~~, 12~~]. These approaches can be quite effective at determining the final state of damage; however, they often cannot provide information about how a given state of damage initiated or evolved during the test. Because of this limitation, initiation and propagation of damage is often indirectly inferred from observed nonlinearities and sudden changes in the specimen's structural response. To address this limitation, some studies have leveraged recent advances in laboratory-scale and synchrotron-radiation X-ray CT imaging to perform in-situ progressive-damage testing of FRCs in near real-time [12]. In-situ testing has been enabled by the accelerated rate at which X-ray images can be acquired, and the development of novel in-situ mechanical load frames [13]. To date, in-situ X-ray CT imaging of damage evolution during mechanical loading has been performed on unnotched [13-15], edge-notched [16-18], and open-hole [19] polymeric- and ceramic-matrix FRC specimens. In all of these cases, X-ray CT imaging has revealed a wealth of previously unavailable 3D information, which has challenged the current understanding of how damage initiates and evolves in FRC test articles prior to macroscopic failure [12]. In particular, high-resolution X-ray CT imaging has provided new insight into initiation and evolution of constitutive-level damage mechanisms (e.g., tensile and shear-driven microcracking, fiber bridging, fiber pullout), which are important energy-dissipative mechanisms that are often ignored in existing ply-level PDA models. Further understanding of these mechanisms, and full accounting of all processes occurring during progressive damage testing, may ultimately address some of the existing disparities between PDA simulations and experiments.

Considering the above discussion, this work aims to advance the existing framework used to study damage evolution in FRCs by incorporating in-situ X-ray CT imaging and testing. To date, in-situ X-ray CT imaging has been applied to uniaxial tensile testing as described in Refs. [13-19]. However, FRC structures are seldom subject to exclusively tensile loads. Flexural loading results in a more complex state of stress across the specimen's thickness, which may be more consistent with structural applications of FRCs. Flexural loading produces a specimen response, and corresponding fracture patterns, that are vastly different from those observed in uniaxial tension tests. Therefore, in this work we use in-situ X-ray CT imaging to investigate failure under flexural loading conditions. In addition to in-situ imaging, this study investigates several new methods of image analysis. Overall, this work is expected to provide detailed information about the geometry of tape laminates, as well as an in-depth understanding of how fracture initiates and evolves through laminates loaded in flexure.

A novel vertical-flexure test apparatus is presented, which is designed to interface with an existing loading stage (see Ref. [13]) at the Advanced Light Source (ALS) tomography beamline 8.3.2 (Lawrence Berkeley National Laboratory, Berkeley CA). The new flexure apparatus is designed to provide an unobstructed view of the sample gage region during in-situ testing, which dramatically improves the X-ray CT image quality. The proposed method is evaluated by testing and imaging tape-laminate specimens with two distinct stacking sequences. The first stacking sequence, with a quasi-isotropic layup, is designed to elicit interaction between transverse fracture and delamination growth. The second stacking sequence is designed to contain small angular changes between adjacent plies to promote extensive growth and migration of transverse cracks through the specimen thickness. Several segmentation and visualization methods are implemented and used to produce information necessary for validating high-fidelity PDA simulations.

2. Experimental Methodology

2.1 In-situ flexure apparatus

In-situ testing imposes inherent restrictions on geometry and size of the specimen and the testing apparatus. To achieve high-quality CT images without needing to modulate X-ray energy [20] or using advanced reconstruction algorithms [21, 22], the gage region of the specimen must be uniform and unobstructed through all angles of rotation required for tomographic imaging. A standard flexure test, wherein the length of the specimen is aligned perpendicular to the loading direction, will have drastically different X-ray attenuation when the specimen is end-on versus side-on to the incoming X-ray beam. A large aspect ratio of support length to specimen thickness accentuates this problem, which can cause artifacts in the image during tomographic reconstruction [23].

To avoid imaging issues associated with horizontal flexure testing, a novel test configuration, shown in Fig. 1, was developed in collaboration with authors of Ref. [24], where the flexure specimen is oriented vertically (i.e., length is perpendicular to the incoming X-ray beam) and the bending is applied using two eccentric compressive loads.

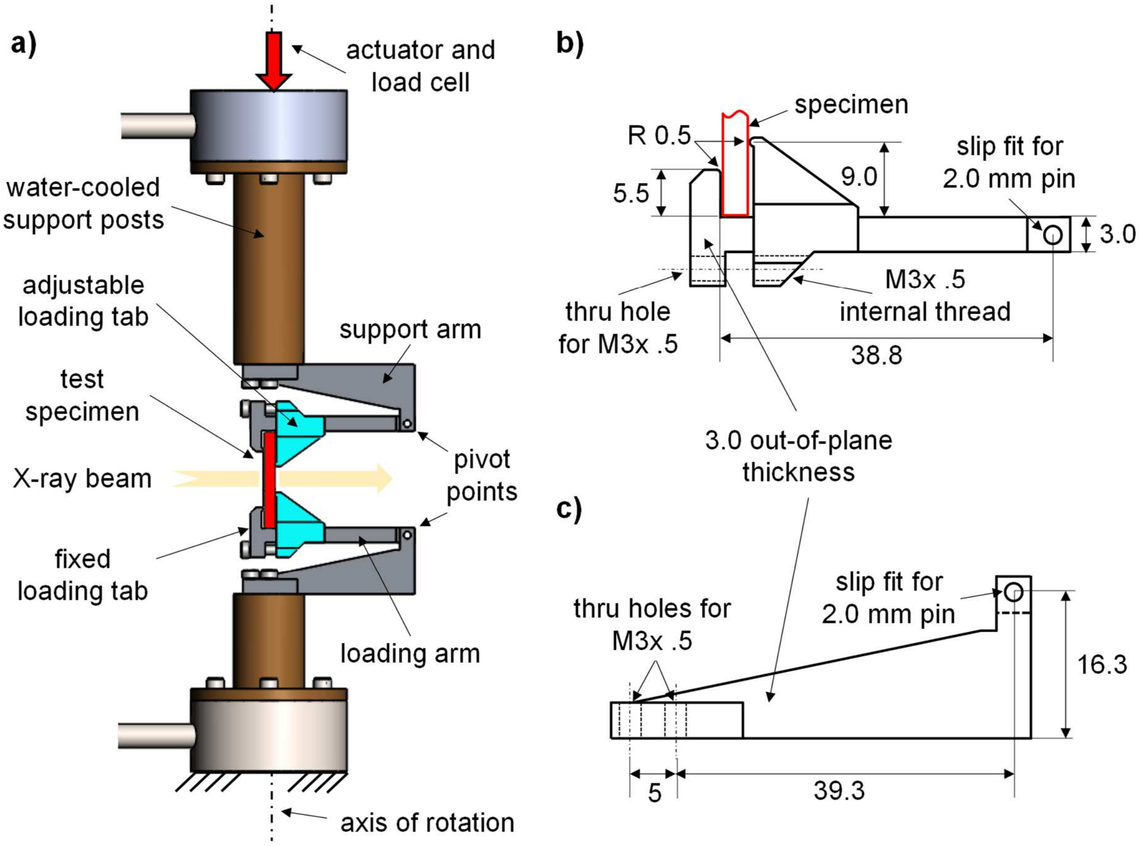

Figure 1. The vertical flexure test setup and dimensions of the loading and support arms. All units in mm.

As seen in Fig. 1a-b, the vertically oriented specimen is held in place using grips consisting of two sets of fixed and adjustable loading tabs, which are located on the left side of the loading arms and tightened using two M3x0.5 screws. The loading arms are connected to the fixed support arms (see Fig. 1a, c) using 2.0 mm diameter pins. The fixed arms are connected to the load frame base and the actuator/load-cell assembly using water-cooled support posts. When gripped using loading tabs, the specimen creates a rigid connection between the upper and lower parts of the fixture. With this assembly, a downward displacement of the upper support arm causes rotation of the loading arms around the pivot points (see Fig. 1a), which in turn imparts bending and slight compression onto the composite specimen. The net effect of this loading is lateral flexure and downward translation of the specimen. In the setup shown in Fig. 1a, the left and right faces of the specimen experience tensile and compressive stresses, respectively.

The overall geometry and size of the fixture shown in Fig. 1 were selected based on several test requirements and geometrical constraints. First, the entire flexure apparatus was designed to interface with an existing in-situ ultra-high temperature load frame [13] at the ALS tomography beamline 8.3.2. The fixture and specimen configuration was sized such that, at the maximum expected downward translation, the specimen's central region of interest (ROI) remained in the field of view (FOV) provided by the 7 mm tall X-ray transmission window of the load frame. Moreover, the support and loading arms were sized to limit the compressive force imparted onto the specimen, which resulted in approximately 5% difference between tensile and compressive strains, as determined by exploratory ex-situ tests and digital image correlation (DIC) analysis. To extend the use of this setup to other high-performance materials and test environments, such as ceramic matrix composites, the dimensions of the fixture were sized to ensure unobstructed specimen heating using six infrared heat lamps mounted within the chamber [13]. Additionally, all parts of the flexure apparatus were machined from MAR M247 super-alloy using wire electrical discharge machining, while the water-cooled support posts were made from phosphor bronze.

2.2. Specimen design and fabrication

Two different laminate stacking sequences were designed for this study. The first stacking sequence, $[0_2/90_2/(\pm 45)_2]_S$, was designed with large relative angles ($\Delta\theta$) between adjacent plies, which promotes combined delamination growth and transverse fracture [25]. The second stacking sequence, $[0_3/90/75/60/45/30]_S$, was designed with small $\Delta\theta$, to encourage formation and growth of periodically-spaced transverse cracks across ply interfaces with limited delamination [25]. Throughout the remainder of this paper, the two stacking sequences will be referred to as large angle (LA) and small angle (SA), respectively.

Both laminates were manufactured using 190 gsm areal weight IM7/8552 carbon/epoxy tape-laminate prepreg cured in a hot press according to the manufacturer's recommended cure cycle [26]. After curing, the two laminates were sectioned using a diamond blade saw to create the specimen geometry shown in Figure 2. All specimens were nominally 3.0 mm wide, 2.8 mm thick, and 26 mm long. The specimen cross sectional area was dictated by the desired imaging resolution and corresponding FOV provided by optics of beamline 8.3.2.

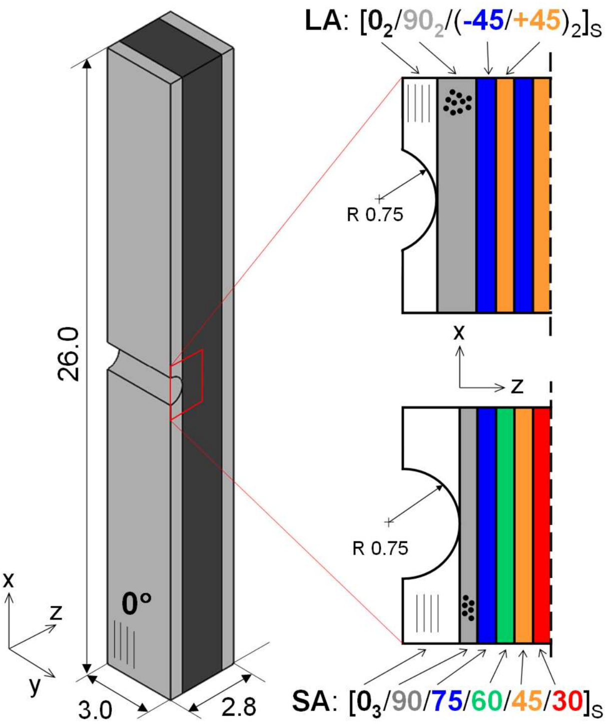

Figure 2. Geometry and stacking sequences of the large (LA) and small (SA) angle flexure specimens (units in mm).

As seen in Figure 2, both stacking sequences included 0° plies (i.e. aligned with the beam length) on the top and bottom surfaces. These plies were needed to increase the overall flexural rigidity of specimens and decrease the horizontal displacement at the onset of fracture. To encourage damage initiation in the central gage region, a 0.75 mm diameter semi-circular notch was machined, using a diamond-coated blade, into each specimen through the 0° plies on the tensile side. The notch ensured that fracture initiated with a width-wise transverse matrix crack in the 90° ply, which subsequently encouraged damage formation in the adjacent ply from a naturally occurring sharp crack front.

2.3. In-situ testing and X-ray CT imaging

In-situ testing and X-ray CT imaging was conducted at the ALS beamline 8.3.2. Prior to mechanical testing, all specimens were scanned in the gage region to obtain baseline X-ray CT images. Three specimens per stacking sequence were tested using displacement control at a rate of 0.5 mm/min. Sample failure was monitored using live X-ray projections in the fluoroscopy imaging mode. For each stacking sequence, two specimens were monotonically loaded until the internal damage emanating from the starter notch reached the edges of the available FOV. These specimens were subsequently held at a constant displacement and scanned to obtain X-ray CT images. For the remaining specimen, X-ray CT images were collected after every notable damage event, resulting in a set of multiple X-ray CT images. Notable damage events were identified either from changes in the live X-ray projection, or from sudden drops in the load.

All imaging was done in a white light mode by acquiring 2048 projections each with a 250-500 ms exposure time. A 5× objective lens was used for all scans, which resulted in a 3.3 mm × 3.3 mm field of view, 2.8 mm image stack depth, and a cubic voxel size of 1.3 μm. Depending on the extent of damage, multiple tomographic scans were tiled vertically, and combined into one stack after reconstruction. In total, 25 scans were performed, producing over 500 GB of raw 32-bit image data. Tomographs for each scan were reconstructed using filtered back-projection with TomoPy, an open-source tomographic data processing and image reconstruction software package [27]. A few examples of post-reconstruction tomographic images are provided in Section 1 of the Supplementary Information document. Cropping and alignment of the image stacks prior to segmentation was done using ImageJ [28].

After testing and imaging at the ALS, additional four specimens per geometry were tested ex-situ at the Utah Composites Laboratory (UCL). This was done to measure the overall compliance of the test setup and obtain additional force-displacement curves.

2.4 Segmentation of X-ray CT images

Segmentation of X-ray CT images was performed to extract information about the ply structure of each specimen (i.e., local ply thickness and fiber orientation), and to determine the evolution of damage resulting from flexural loading. Segmentation of ply structure was done using an open-source ImageJ plug-in, OrientationJ [29]. Prior to segmentation, all image stacks were re-sliced in ImageJ such that the z-direction (see Fig. 2) was the new stack direction (i.e., the resliced tomographic images were in the x-y plane). An example of one such image, extracted from the SA specimen, is shown in Fig. 3a. As seen in this figure, the scan resolution is high enough to visually identify direction of individual fibers or fiber clusters. More specifically, there are approximately 4 voxels across an average diameter of a typical IM7 fiber. Given the visible directionality of individual fibers, OrientationJ plug-in was used to calculate the structure tensor, J, in a local ROI surrounding each pixel location within each tomographic image. Given J for each pixel, OrientationJ calculates the predominant orientation, θ, and coherency, C, of the image contained within the corresponding ROI. A value of C close to 1 indicates a dominant orientation, while C close to zero indicates lack of directionality. As a result of calculating J, local orientation of fibers can be determined using θ, while regions containing pores or pure resin can be extracted using low values of C. An example of calculating θ for the image in Fig. 3a is shown in Fig. 3b. In this figure, the colors are in the hue/saturation/brightness (HSB) color space (see Fig. 3c) and indicate local fiber direction, as defined in Fig. 3c. As seen in Fig. 3b, OrientationJ easily isolates the two dominant ply orientations (+45° and +60°), as well as the small region of pure resin. The image analysis shown in Fig. 3b was performed for each tomographic stack using a local ROI of 5x5 pixels. This information was then used to isolate individual plies within each laminate. For each ply, local ply thickness was calculated by measuring the z-direction distance between pixels on the top and bottom surface at each x-y pixel coordinate. For brevity, voids and resin rich regions were excluded from further segmentation and analysis.

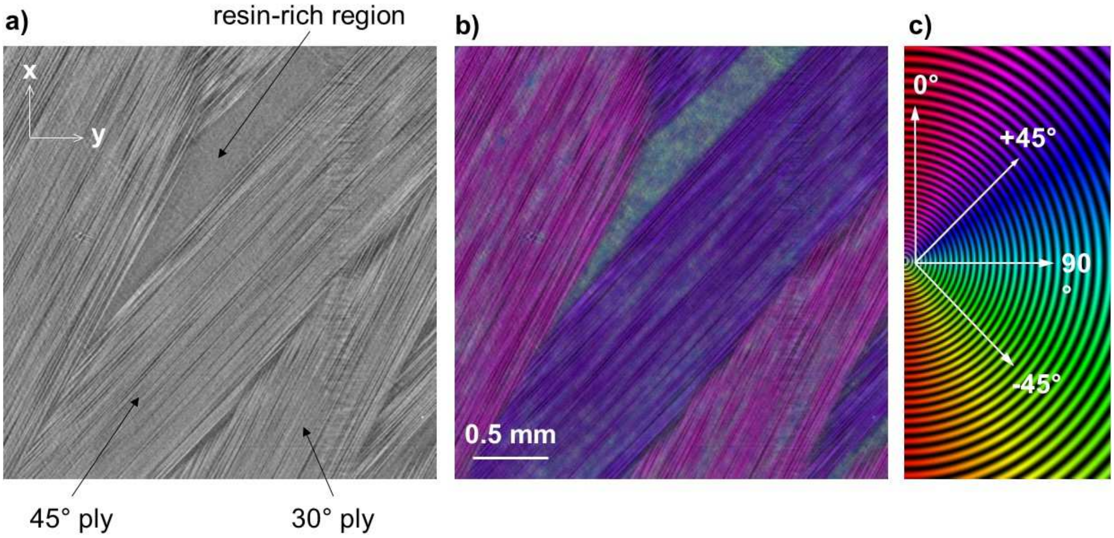

Figure 3. Example of (a) a typical tomographic image from the SA specimen, and (b) the corresponding fiber orientation determined using the OrientationJ plug-in in ImageJ. In above, (c) defines the angle orientation in (b) using the HSB color space.

Segmentation of damage, which involved selection of transverse cracks and delaminations, was done using semi-automated greyscale thresholding with a commercially available software Avizo (FEI Visualization Sciences Group). In Aviso, grayscale thresholding was used to automatically select voxel networks that corresponded to the damage. This was followed by manual pixel selection, which was necessary to select isolated damage regions that failed to segment due to discontinuities in the crack networks or reconstruction artifacts. Once segmented, all cracks and delaminations were manually categorized and color-coded in Avizo according to damage type and location within the laminate. In the subsequent discussion, results will be shown for one representative specimen per laminate type. Results from segmenting additional specimens are given in Section 2 of the Supplementary Information document.

3. Results and Discussion

3.1. Segmented ply structure

The segmented ply-level structure of LA and SA specimens is shown in Figure 4. In this figure, the machined notch is visible on the left-hand side of each volume, and the grayscale colors correspond to plies segmented using the OrientationJ plug-in described in the previous section.

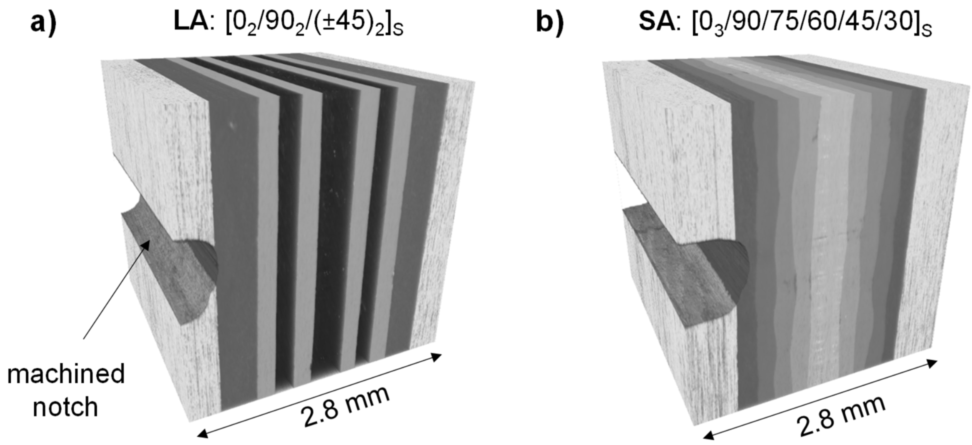

Figure 4. Example of the segmented ply-level structure of the (a) LA and (b) SA specimens. The grayscale colors represented individual plies.

Examining Figure 4, the thickness of individual plies in the LA specimen is relatively uniform compared to plies in the SA specimen. In the SA specimen, the extent of ply waviness appears to be related to the $\Delta\theta$ between adjacent plies. For instance, the neighboring plies with a large $\Delta\theta$ (e.g., 0°/90°) close to the free surface are relatively uniform, while plies with small $\Delta\theta$ (e.g., 75°/60°, 60°/45°, 45°/30°) become increasingly wavy towards the interior of the laminate. The quantitative measure of the through-thickness ply waviness for LA and SA specimens is presented in Figure 5a and 5c, respectively. In the plots shown, the nominal ply angles are indicated on the horizontal axes according to the corresponding stacking sequence, while the measured ply thicknesses are given on the vertical axes. Blocks of plies with the same orientation are grouped and treated as a single ply. For each ply in Figure 5a and 5c, the gray boxes represent the 25^{th}, 50^{th}, and 75^{th} percentiles of the measured thickness, while the whiskers represent the 5^{th} and 95^{th} percentiles. Examining Figure 5a, the LA specimen exhibits little scatter in ply thickness, with average single-ply thicknesses ranging between 0.15 and 0.20 mm and clustering largely around 0.169 mm (which is close to the expected nominal thickness of cured the

IM7/8552 prepreg [26]). The distribution of ply thicknesses in the SA specimen, shown in Figure 5b, is less uniform, with most of the nonuniformity occurring in the 30°, 45°, 60° plies. Similar to the LA specimen, the average ply thickness of the SA specimen is approximately 0.166 mm; however, the range of thicknesses is nearly triple that of the LA laminate. Based on present analysis, the actual mechanism that causes ply nonuniformity/waviness in the SA specimen is unclear, but it is likely related to the relative stiffness of the uncured plies and their interaction during initial consolidation and cure. Regardless of the mechanisms causing the through-thickness ply waviness in the SA specimen, the data in Figures 4b and 5c suggest that ply waviness may need to be considered in ply-level simulations of damage in tape-laminates, especially if certain input parameters (e.g., in-situ transverse tensile strength, Ref. [30]) are strongly depended on the local ply thickness.

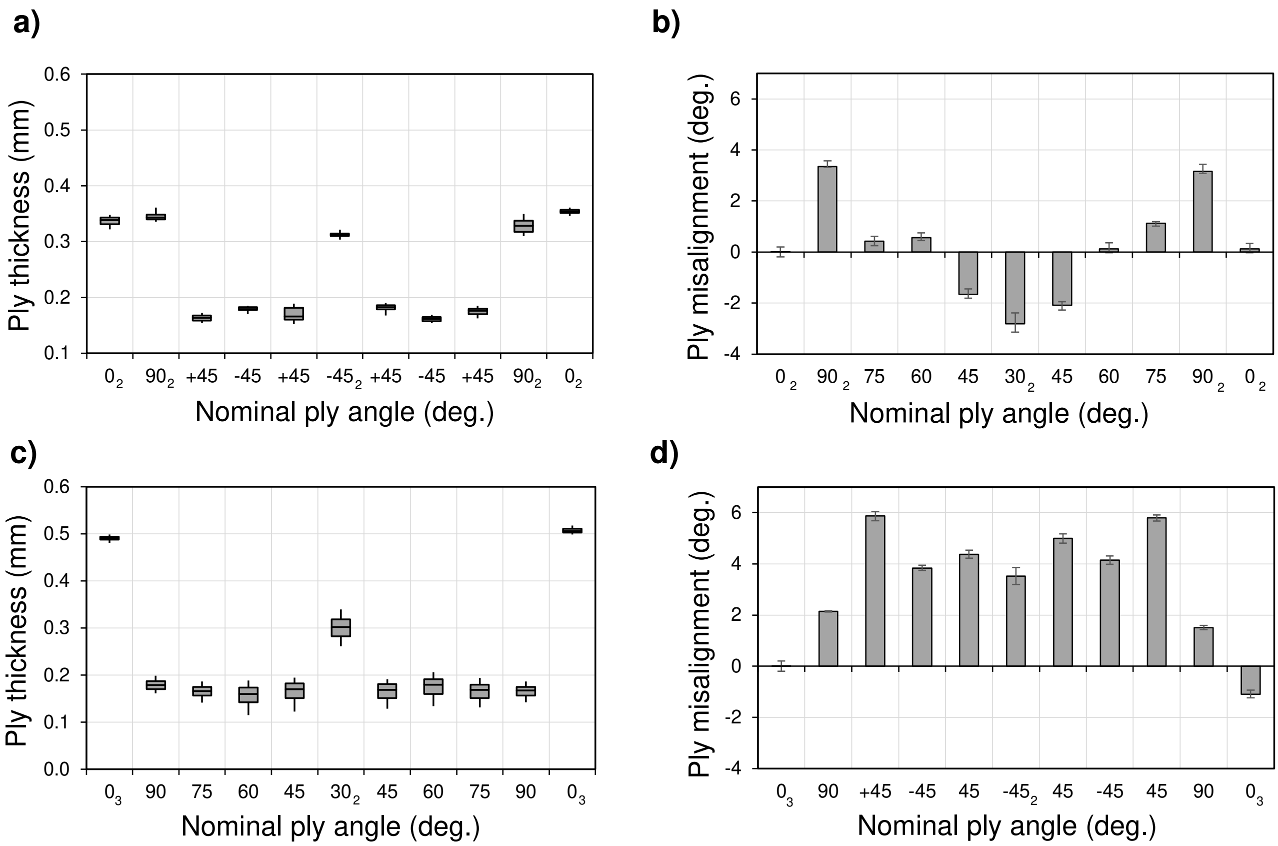

Figure 5. Summary of ply thickness and local in-plane fiber misorientation measurements for LA (a,b) and SA (c,d) laminates.

In addition to thickness waviness, each ply in the LA and SA specimens was analyzed to determine the local in-plane fiber misorientation relative to the nominal/expected ply angle. A summary of this analysis is presented in Figures 5b and 5d, where the horizontal axes indicate the nominal (or expected) ply angle, and the vertical axes given the difference between nominal orientation and the average measured fiber orientation in each ply. Examining Figures 5b and 5d, all measured fiber orientations are within 4-6° from the nominal values, and the maximum standard deviation in fiber orientation is 0.33° and 0.41°, for the LA and SA specimens, respectively. The observed variations from nominal ply angles are not entirely unexpected and are likely the result of manual ply cutting and hand layup. The low standard deviation in fiber orientation within each ply, relative to the overall ply misorientation, is perhaps indicative of good manufacturing processes used during fiber pre-impregnation.

Overall, the analysis presented in this section suggests that ply thickness and orientation in tape-laminates can be different from the nominal/assumed values. These variabilities may require further attention, especially in the context of comparing numerical predictions of deformation and damage to those obtained from experiments. The high-quality segmentation data obtained using the OrientationJ plug-in may enable development of ply-level FE models where variability in ply thickness and material stiffness (e.g., assigned according to local fiber orientation) can be represented explicitly. See Ref. [31] for an example of converting X-ray CT images into detailed FE meshes.

3.2 Force-displacement responses

The force versus vertical displacement responses from testing the LA and SA specimens are shown in Figures 6a and 6b, respectively. In these plots, the solid black curves correspond to the LA and SA specimens on which detailed image analysis was performed as described in the subsequent sections. The gray curves correspond to additional specimens that were tested and imaged in situ at the ALS (solid gray lines) and tested ex situ at the UCL (dashed gray lines). In Figure 6, the solid red circles correspond to force-displacement pairs at which the loading was paused and the corresponding specimen was imaged. The number next to each red dot corresponds to displacement value prior to pausing the test for imaging. The open circles indicate the final force-displacement pairs at which the additional specimens were imaged at the ALS.

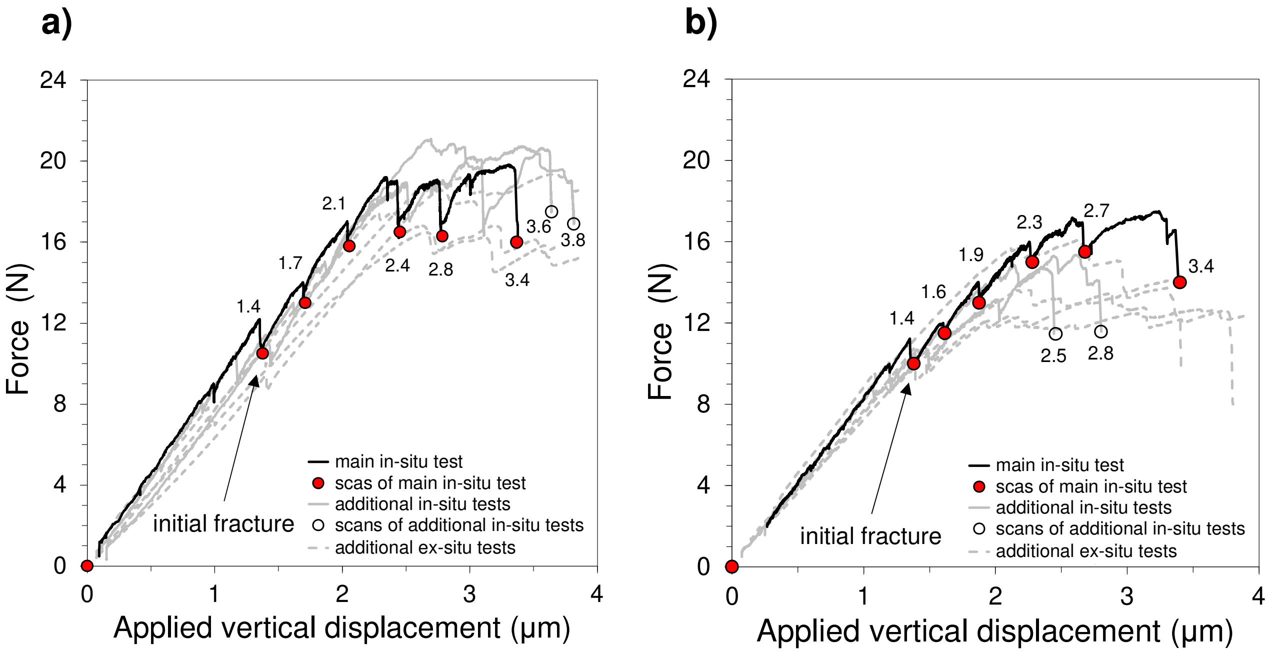

Figure 6. Force versus vertical displacement response of LA (a) and SA (b) specimens. The solid black lines correspond to the specimens described in the results section. The gray lines correspond to additional specimens tested *in situ* at the ALS (solid) and *ex situ* at the UCL (dashed). The individual numbers indicate the displacement value at which the specimens were paused for scanning.

Examining the curves in Figure 6, both groups of specimens exhibited a linear force-displacement response prior to onset of fracture. For both specimen types, fracture initiated at approximately 1.4 mm of displacement, which is indicated by the first major load drop. The small load drops prior to 1.4 mm of displacement did not correspond to detectable damage in the live X-ray projections. As will be described in the next two sections, the first load drop corresponded to fracture of the 90° plies along the length of the machined notch, followed by secondary fracture in the adjacent plies. After the initial fracture, the two specimen types exhibited slightly different behavior. The response of the LA specimens remained relatively linear up to the peak load, exhibiting a few large load drops along the way. After reaching the peak load, the specimen response plateaued, exhibiting load drops that were larger in magnitude than those during the initial loading. As will be shown in the following two sections, the sudden load drops corresponded to sudden formation of new, or extension of existing, fracture surfaces. The response of the SA specimens was only linear up to the first major load drop, upon which, the response gradually softened as more damage accumulated away from the machined notch. Similar to the LA specimens, the magnitude of major load drops appeared to increase with the increasing load.

Overall, comparing the in-situ and ex-situ test data in Figure 6, the response of both layup types was repeatable and consistent; however, the occurrence of large load drops varied somewhat from specimen to specimen. As described in the Supplementary Information document, this variability likely stems from the way in which fracture evolved throughout each specimen and may be related to the internal ply structure (see section 3.2), the stochastic distribution of material properties, or specimen misalignment.

3.3 Evolution of fracture surfaces in the LA specimen

The evolution of fracture surfaces in the LA specimen is shown in Figure 7 at the displacement values defined in Figure 6a. In all six sub-figures the color scheme identifies the location of damage within the laminate as defined in the legend. Specifically, the red, blue, and fuchsia colors define intralaminar cracks in the 90°, +45°, and -45° plies, respectively. The green and yellow colors correspond to delaminations at the 90°/+45° and the +45°/-45° interfaces, respectively. Finally, the semi-cylindrical gray features in each sub-figure correspond to the empty space occupied by the machined notch. The same evolution of fracture is visualized using three-dimensional rendering in the corresponding Video 1.

Examining Figure 7a, the progression of internal damage in the LA laminate begins with formation of a single transverse crack in the 90° plies that spans the entire specimen width. This fracture is accompanied by formation of a few short transverse cracks in the adjacent +45° ply. As the load is increased, the frequency and length of transverse cracks in the +45° ply increases and there appears to be some evidence of delaminations forming at the 90°/+45° interface (see Fig. 7b) between the widthwise crack in the 90° ply and individual short cracks in the 45° ply. It is interesting to note that transverse cracking in the +45° ply precedes delamination growth at 90°/+45° interface, and not the other way around. At the next imaging increment (Fig. 7c), seven dominant transverse cracks in the +45° ply extend outward, and that seems to suppress initiation and growth of additional cracks in the +45° ply. The extension of the dominant transverse cracks is accompanied by further, albeit subtle, delamination growth at the 90°/+45° interface. The next large load drop, at approximately 2.4 mm of displacement (Fig. 7d), results in large extension of delaminations at the 90°/+45° interface, and some delamination growth at the +45°/-45° interface. The delamination at the +45°/-45° interface appears to be bounded by the outermost transverse cracks in the +45° ply and the specimen's edges. As shown in Figs. 7e-f, additional loading results in further extension of the transverse cracks in the +45° ply, growth of delaminations at the 90°/+45° and +45°/-45° interfaces, and some transverse cracking in the -45° ply. The final state of damage, depicted in Fig. 7f, is very similar to the damage observed in the two additional specimens tested and imaged at the ALS, as shown in Section 2 of the Supplementary Information document. It should be noted that in all three specimens imaged, the inter- or intralaminar damage never extended past the midplane, and majority of fracture was contained below the +45°/-45° interface. Finally, although not shown in Fig. 7, almost all intralaminar cracks in the LA specimens exhibited some fiber bridging (see Fig. S1 in the Supplementary Information document), which is consistent with observations in Ref. [32]. The presence of fiber bridging may explain why certain transverse cracks failed to extend during the loading, but further quantification of this behavior is outside the scope of this work. Nevertheless, presence of fiber bridging during transverse fracture appears to be an important mechanism that may require further attention in progressive damage simulations of tape laminates.

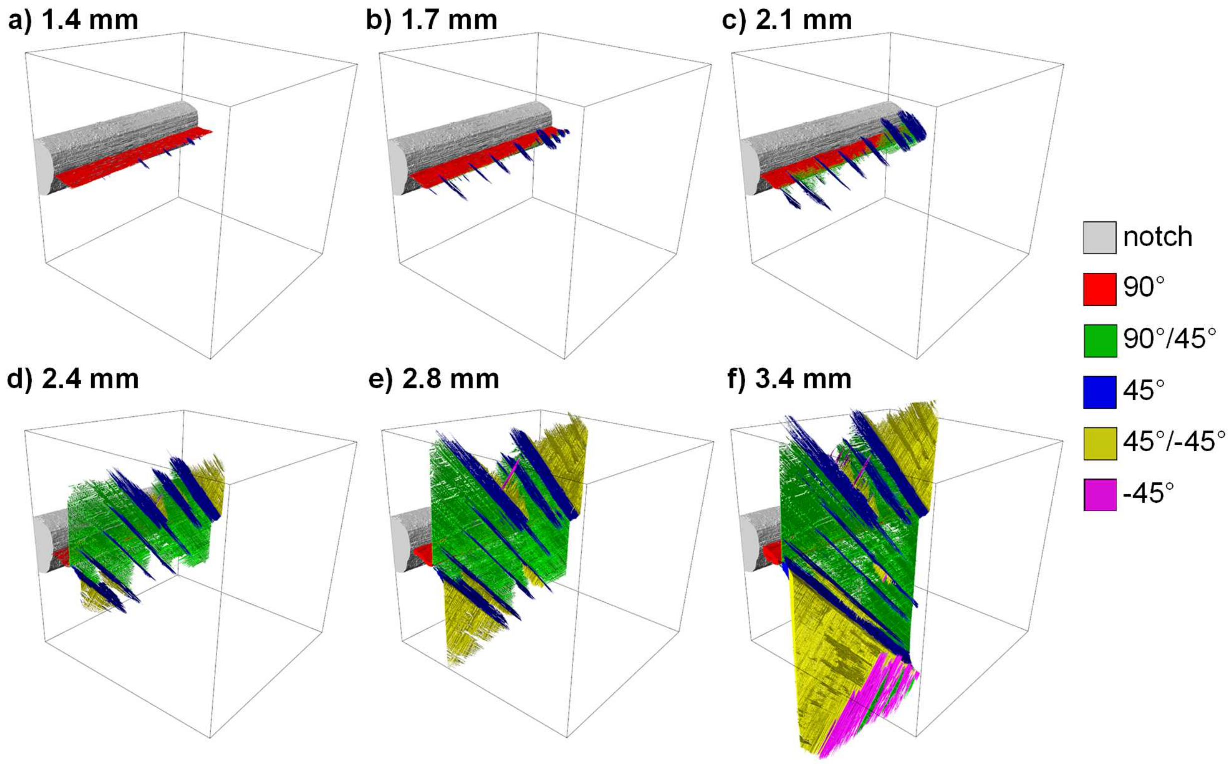

Figure 7. Evolution of fracture surfaces in the LA specimen at the displacement values defined in Figure 6a. The gray semi-cylindrical feature in each subfigure corresponds to the empty space occupied by the machined notch.

3.4 Evolution of fracture surfaces in the SA specimens

The evolution of damage in the SA specimen, shown in Figure 8 and Video 2, is markedly different from what was observed with the LA specimens. As shown in Fig. 8a, initiation of damage in the SA specimen begins with a widthwise fracture of 90° ply, followed by a simultaneous formation of short, densely spaced, transverse cracks in the 75°, 60°, and 45° plies. From the present analysis, it is not immediately obvious why fracture propagated so rapidly through the first four plies; however, is very likely that this advance was caused by a) an accumulation of excess strain energy at the relatively blunt notch, and b) a relatively low resistance of the 90°, 75°, 60°, and 45° plies to through-thickness transverse fracture. In the SA specimen, cracks in the 60° ply always initiated from cracks in the 75° ply, and cracks in the 45° ply always initiated from cracks in the 60° ply. In other words, all transverse cracks initiated from stress/strain concentrations caused by fracture in neighboring plies. It should be noted that not all cracks in the 75°-ply initiated damage in the adjacent 60° ply, and there is visible transverse crack coarsening moving from the 75° ply towards the midplane. Examining Fig. 7, it appears that the frequency and density of transverse cracks is inversely proportional to the distance away from the notch, with most of the cracking occurring in the 75° ply. Despite this coarsening, there is a clear set of connected crack paths starting at the notch and spanning the 90°, 75°, and 60° plies. Contrary to what was observed in the LA specimens, the inward growth of these initial crack paths, from one ply to the next, always occurred without delamination growth at a given interface. This type of growth has been observed in other studies (e.g., see Refs. [25, 33]), and is likely related to the small $\Delta\theta$ between adjacent plies.

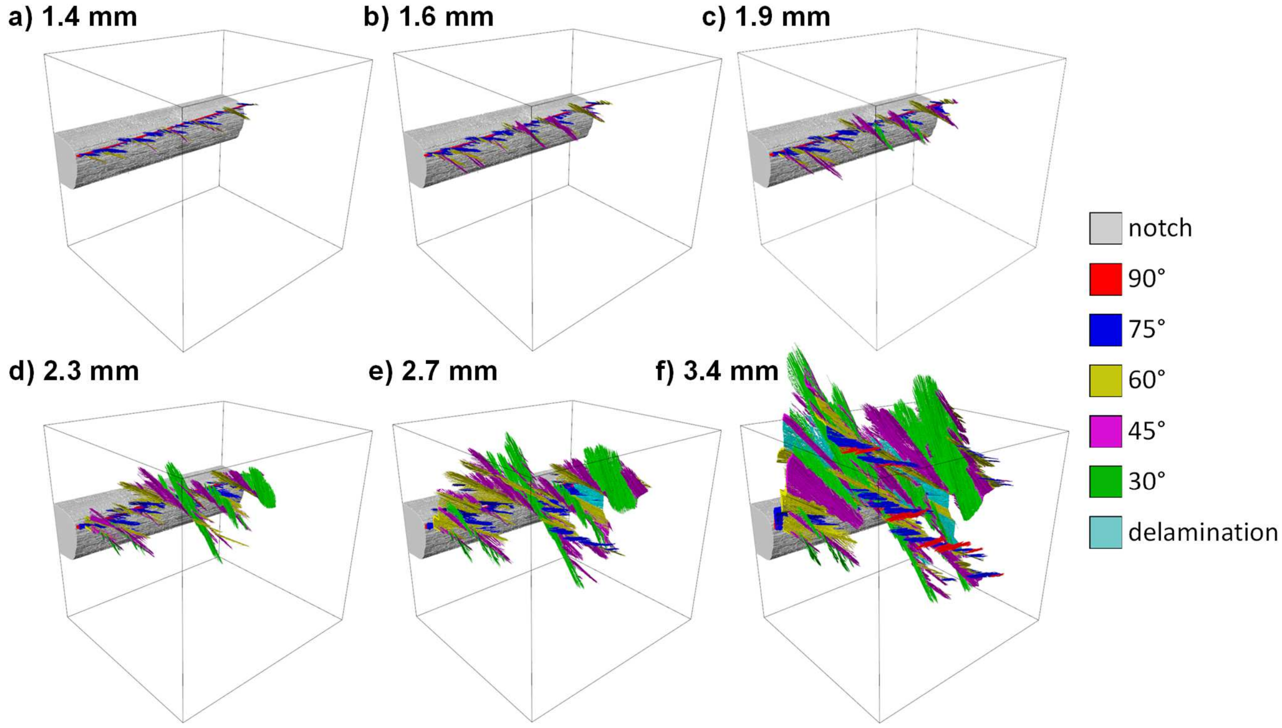

Figure 8. Evolution of fracture surfaces in the SA specimen at the displacement values defined in Figure 6b. The gray semi-cylindrical feature in each subfigure corresponds to the empty space occupied by the machined notch.

Examining Figs. 8b-e, additional loading of the specimen results in extension of existing transverse cracks, and formation of new cracks in the 45° and 30° plies on both sides of the midplane. As evident from these figures, each fractured ply contains several dominant cracks which a) become longer as the loading is increased, and b) are responsible for initiating new transverse cracks in the adjacent plies. In a few instances, these dominant cracks result in transverse cracks on each side of the corresponding ply. At the final load increment, shown in Fig. 8f, a few large delaminations are observed near the midplane; however, these seemed to form only after several dominant transverse cracks have reached the free edges of the specimen. As in the LA specimens, the final state of damage in Fig. 8f has a similar form to the damage in the additional two specimens tested and imaged at the ALS (see Section 2 of the Supplementary Information document).

In is noted that the above discussion provides a qualitative explanation of damage evolution in the SA specimen during flexure loading. To offer additional insight into how transverse cracks evolve and interact during specimen loading, an alternative way of visualizing damage evolution is presented in Section 3 of the Supplementary Information document.

3.5. Discussion of damage evolution in the LA and SA specimens

The intent of testing LA and SA specimens in this work was to demonstrate the utility of the vertical flexure experiment, and to show that vastly different states of damage can be achieved by changing the relative angles between adjacent plies. Accordingly, as described in Sec. 3.3, the LA specimens exhibited a state of damage that was dominated by a combined growth and interaction of intralaminar cracks and delaminations. Because of the 90° angle change at the +45°/-45° interface, the internal damage was largely contained to one side of the laminate thickness, which highlights the relative resistance of the LA stacking sequence to through-thickness damage growth. In contrast, damage in the SA specimens was dominated by intralaminar fracture, which seemed to corkscrew into the laminate along several dominant crack paths distributed along specimens' width. These crack paths extend from the machined notch well beyond the midplane, and suggests that the SA laminate, containing small $\Delta\theta$s between adjacent plies, has low resistance to through-thickness damage growth. Overall, the in-situ flexure experiments reveal that fracture in tape laminates, regardless of stacking sequence, is a rather complex process that results in a wide range of different-size cracks with a noticeably uneven/jagged fronts. Although this observation is not new, and has been reported in other similar studies [13-18], it further motivates development of new tests that evaluate how existing numerical models approximate real physical phenomena of fracture in tape laminates.

3.6 Assessment of the vertical flexure experiment

The experimental data presented in the proceeding sections can be used to provide a preliminary assessment of the vertical flexure experiment. Overall, the test provided a relatively clear view of progressive damage evolution in the two specimen types. The X-ray CT images did not exhibit any major artifacts caused by in-situ loading, while the image resolution was high enough to resolve individual fibers and intricacies of individual inter- and intralaminar cracks. Moreover, the LA and SA specimen configurations behaved as intended, evolving vastly different fracture patterns that were clearly depended on the respective stacking sequences. One aspect of the specimen design that requires further attention is the unstable onset of initial fracture, where damage progressed through multiple plies before the first Xray CT scan was performed (see Figs. 7a and 8a). The unstable progression of damage was likely caused by the large notch radius, which caused accumulation of excess strain energy in the 90° ply, resulting in unstable release and rapid damage progression into the adjacent plies. To slow down the development of damage emanating from the 90° ply, higher-quality and sharper notches may be required. This can likely be achieved by combining more precise machining of the 0° plies and subsequent fatigue pre-cracking of the 90° plies.

One of the biggest and partially unresolved challenges in this study was the analysis of the X-ray CT images. As described in Section 2.4, segmentation of various features in the X-ray CT images was performed either manually or semi-automatically, which stemmed from lack of image analysis tools that would automate the entire process. The existing segmentation and analysis tools are inadequate for an exhaustive image analysis that include quantification of intralaminar fiber bridging, crack face opening and sliding, crack growth rate and evolution of crack surface area, to name a few. Improved automated analysis tools which can provide more detailed information may be necessary for further development and validation of existing PDF methodologies. A recent emergence of machine learning (ML) algorithms for image analysis may provide a new avenue for automating and improving segmentation of the data presented in this work. The reader is directed to Ref. [34] which highlights benefits of ML approach for feature segmentation in X-ray CT images.

4. Conclusions

In this study, an in-situ flexure test was developed for imaging progressive inter- and intralaminar fracture in tape-laminate composites using X-ray computed tomography (CT). The intent of this test was to provide detailed experimental observations of ply-level damage that can be used to validate existing, and develop new, progressive damage analysis (PDA) tools. The test consisted of a vertically mounted specimen which was flexed using two eccentric compressive loads using an in-situ uniaxial load stage. The flexure specimen contained a starter notch mid-span which promoted initiation of through-thickness fracture within the field of view. Functionality of the proposed method was evaluated by testing and imaging tape-laminate specimens with two distinct stacking sequences. The first stacking sequence was designed to elicit interaction between transverse fracture and delamination growth. The second stacking sequence was designed to contain small angular changes between adjacent plies to promote extensive growth and migration of transverse cracks through the specimen thickness. Several segmentation and visualization methods were implemented to produce information necessary for generating and validating high-fidelity finite element (FE)-based PDA simulations. Based on the results presented, the key findings from this study are as follows:

- The vertical flexure experiment combined with high-resolution synchrotron-based X-ray CT imaging provides a highly detailed view of the underlying ply structure and the progressive evolution of inter- and intralaminar damage in tape laminates. The vertical orientation of the test specimens enables artifact-free imaging of the gage region, which greatly simplifies feature segmentation from X-ray CT images.

- Based on the results from this study, two major upgrades to the vertical flexure tests are recommended. The first upgrade requires development of a new procedure for creating the starter notch. The starter notch used in this study resulted in an initially unstable fracture process, which for both laminate types tested extended through multiple plies at once. The second improvement requires modification to how the specimen is gripped prior to loading. In the current configuration, the adjustable loading tabs result in additional specimen rotation, which is not easily modeled numerically.
- The X-ray CT data was collected at high enough resolution to enable characterization of local ply thickness and fiber orientation. This characterization revealed that laminates with small relative angles between adjacent plies exhibit higher ply-thickness variability. Overall, both laminate types exhibited some misalignment of individual plies from the nominal orientations, which is likely related to the manual layup used. The ply segmentation procedure presented in this work may enable the development of more accurate ply-level FE meshes of as-manufactured laminates.
- The laminate which contained large angle changes between adjacent plies, exhibited a near simultaneous growth and interaction of transverse cracks and delaminations. The transverse cracks exhibited some amount of fiber bridging, and none of the damage extended beyond the laminate's midplane.
- The specimens containing small angle changes between adjacent plies exhibited extensive transverse cracking that extended well beyond the laminate midplane. In general, the through-thickness growth and migration of transverse cracks occurred without any delamination growth.
- The observations made for both laminate types suggest that the overall appearance and extent of through-thickness crack migration in tape laminates is highly depended on the laminate stacking

sequence and the relative angles between adjacent plies. The X-ray CT images clearly shows that the dominant transverse cracks are often accompanied by smaller cracks. These cracks may not necessarily affect the specimens mechanical response, yet may play an important role in energy absorption during the overall fracture process.

- This study highlights the fundamental utility of in-situ X-ray CT imaging and the ever-present need for automation of the feature segmentation algorithms. Without improvements to these algorithms, segmentation of additional important features, such as fiber bridging, crack opening, fracture surfaces, and others, may not be possible.

Acknowledgments

This work was performed as part of an approved program at the Advanced Light Source (Lawrence Berkeley National Laboratory, Berkeley CA), which is a DOE Office of Science User Facility [contract no. DE-AC02-05CH11231].

References:

1. Chen, B.Y., Pinho, S.T., De Carvalho, N.V., Baiz, P.M. and Tay, T.E., 2014. A floating node method for the modelling of discontinuities in composites. *Engineering Fracture Mechanics*, *127*, pp.104-134.

2. Iarve, E.V., 2003. Mesh independent modelling of cracks by using higher order shape functions. *International Journal for Numerical Methods in Engineering*, *56*(6), pp.869-882.

3. Ling, D., Yang, Q. and Cox, B., 2009. An augmented finite element method for modeling arbitrary discontinuities in composite materials. *International Journal of Fracture*, *156*(1), pp.53-73.

4. Greenhalgh, E.S., “Failure analysis and fractography of polymer composites” Woodbridge Publishing, Ltd., Cambridge, UK, 2009.

5. Aymerich, F. and Meili, S., 2000. Ultrasonic evaluation of matrix damage in impacted composite laminates. *Composites Part B: Engineering*, *31*(1), pp.1-6.

6. Kramb, V.A., John, R. and Stubbs, D.A., 2001. A study of the damage progression from notches in an oxide/oxide ceramic–matrix composite using ultrasonic C-scans. *Composites Science and Technology*, *61*(11), pp.1561-1570.

7. Johnston, P.H., Wright, C.W., Zalameda, J.N. and Seebo, J.P., 2010, October. Ultrasonic monitoring of ply crack and delamination formation in composite tube under torsion load. In *2010 IEEE International Ultrasonics Symposium* (pp. 595-598). IEEE.

8. Hongkarnjanakul, N., Bouvet, C. and Rivallant, S., 2013. Validation of low velocity impact modelling on different stacking sequences of CFRP laminates and influence of fibre failure. *Composite Structures*, *106*, pp.549-559.

9. Pavier, M.J. and Clarke, M.P., 1995. Experimental techniques for the investigation of the effects of impact damage on carbon-fibre composites. *Composites Science and Technology*, *55*(2), pp.157-169.

10. Tan, K.T., Watanabe, N. and Iwahori, Y., 2011. X-ray radiography and micro-computed tomography examination of damage characteristics in stitched composites subjected to impact loading. *Composites Part B: Engineering*, *42*(4), pp.874-884.

11. Schilling, P.J., Karedla, B.R., Tatiparthi, A.K., Verges, M.A. and Herrington, P.D., 2005. X-ray computed microtomography of internal damage in fiber reinforced polymer matrix composites. *Composites Science and Technology*, *65*(14), pp.2071-2078.

12. Garcea, S.C., Wang, Y. and Withers, P.J., 2018. X-ray computed tomography of polymer composites. *Composites Science and Technology*, *156*, pp.305-319.

13. Bale, H.A., Haboub, A., MacDowell, A.A., Nasiatka, J.R., Parkinson, D.Y., Cox, B.N., Marshall, D.B. and Ritchie, R.O., 2013. Real-time quantitative imaging of failure events in materials under load at temperatures above 1,600 C. *Nature Materials*, *12*(1), pp.40-46.

14. Crouch, R.D., Clay, S.B. and Oskay, C., 2013. Experimental and computational investigation of progressive damage accumulation in CFRP composites. *Composites Part B: Engineering*, *48*, pp.59-67.

15. Haboub, A., Bale, H.A., Nasiatka, J.R., Cox, B.N., Marshall, D.B., Ritchie, R.O. and MacDowell, A.A., 2014. Tensile testing of materials at high temperatures above 1700 C with in situ synchrotron X-ray micro-tomography. *Review of Scientific Instruments*, *85*(8), p.083702.

16. Wright, P., Fu, X., Sinclair, I. and Spearing, S.M., 2008. Ultra high resolution computed tomography of damage in notched carbon fiber—epoxy composites. *Journal of Composite Materials*, *42*(19), pp.1993-2002.

17. Wright, P., Moffat, A., Sinclair, I. and Spearing, S.M., 2010. High resolution tomographic imaging and modelling of notch tip damage in a laminated composite. *Composites Science and Technology*, *70*(10), pp.1444-1452

18. Scott, A.E., Mavrogordato, M., Wright, P., Sinclair, I. and Spearing, S.M., 2011. In situ fibre fracture measurement in carbon–epoxy laminates using high resolution computed tomography. *Composites Science and Technology*, *71*(12), pp.1471-1477.

19. Clay, S.B. and Knoth, P.M., 2017. Experimental results of quasi-static testing for calibration and validation of composite progressive damage analysis methods. *Journal of Composite Materials*, *51*(10), pp.1333-1353.

20. Krämer, P. and Weckenmann, A., 2010. Multi-energy image stack fusion in computed tomography. *Measurement Science and Technology*, *21*(4), p.045105.

21. Mohan, K.A., Venkatakrishnan, S.V., Gibbs, J.W., Gulsoy, E.B., Xiao, X., De Graef, M., Voorhees, P.W. and Bouman, C.A., 2015. TIMBIR: A method for time-space reconstruction from interlaced views. *IEEE Transactions on Computational Imaging*, *1*(2), pp.96-111.

22. Parkinson, D.Y., Pelt, D.M., Perciano, T., Ushizima, D., Krishnan, H., Barnard, H.S., MacDowell, A.A. and Sethian, J., 2017, September. Machine learning for micro-tomography. In *Developments in X-Ray Tomography XI* (Vol. 10391, p. 103910J). International Society for Optics and Photonics.

23. Liu, D., Gludovatz, B., Barnard, H.S., Kuball, M. and Ritchie, R.O., 2017. Damage tolerance of nuclear graphite at elevated temperatures. *Nature Communications*, *8*(1), pp.1-9.

24. Maillet, E., Singhal, A., Hilmas, A., Gao, Y., Zhou, Y., Henson, G. and Wilson, G., 2019. Combining in-situ synchrotron X-ray microtomography and acoustic emission to characterize damage evolution in ceramic matrix composites. *Journal of the European Ceramic Society*, *39*(13), pp.3546-3556.

25. Lavoie, J.A. and Adolfsson, E., 2001. Stitch cracks in constraint plies adjacent to a cracked ply. *Journal of Composite Materials*, *35*(23), pp.2077-2097.

26. Hexcel Corporation. HexPly 8552 Product Data Sheet; 2016. http://hexcel.com

27. Gürsoy, D., De Carlo, F., Xiao, X. and Jacobsen, C., 2014. TomoPy: a framework for the analysis of synchrotron tomographic data. *Journal of synchrotron radiation*, *21*(5), pp.1188-1193.

28. Schindelin, J., Rueden, C.T., Hiner, M.C. and Eliceiri, K.W., 2015. The ImageJ ecosystem: An open platform for biomedical image analysis. *Molecular Reproduction and Development*, *82*(7-8), pp.518-529.

29. Püspöki, Z., Storath, M., Sage, D. and Unser, M., 2016. Transforms and operators for directional bioimage analysis: a survey. *Focus on Bio-Image Informatics*, pp.69-93.

30. Camanho, P.P., Dávila, C.G., Pinho, S.T., Iannucci, L. and Robinson, P., 2006. Prediction of in situ strengths and matrix cracking in composites under transverse tension and in-plane shear. *Composites Part A: Applied Science and Manufacturing*, *37*(2), pp.165-176.

31. Creveling, P.J., Fisher, J., Dahlkamp, C. and Czabaj, M.W., 2021. Modeling As-Manufactured Fiber-Reinforced Microstructures Based on X-ray Microcomputed Tomography. *Composites Science and Technology*, p.109004.

32. Czabaj, M.W. and Ratcliffe, J.G., 2013. Comparison of intralaminar and interlaminar mode I fracture toughnesses of a unidirectional IM7/8552 carbon/epoxy composite. *Composites Science and Technology*, 89, pp.15-23.

33. French, J., Dahlkamp, C. and Czabaj, M., 2020. Formation of cryobiaxial-induced damage in tape-laminate composites. *Composite Structures*, 235, p.111816.

34. R. Kopp, "X-ray Micro-Computed Tomography and Deep Learning Segmentation of Progressive Damage in Hierarchical Nanoengineered Carbon Fiber Composites," *Ph.D. Thesis*, Massachusetts Institute of Technology (MIT), June 2021.

Internal damage in a tape-laminate with large angle changes between adjacent plies

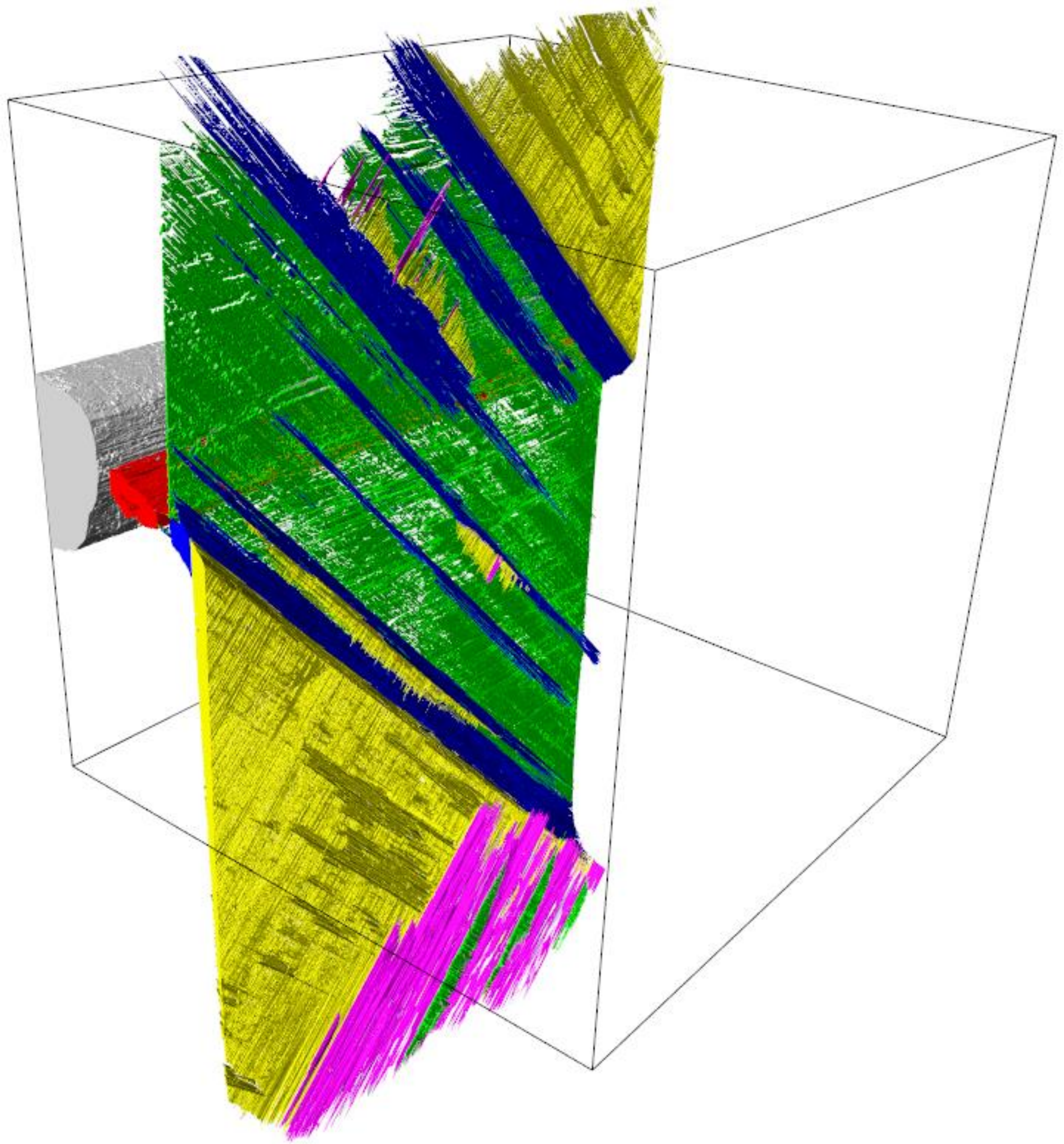

Internal damage in a tape-laminate with small angle changes between adjacent plies